Histidine-Mediated Synthesis of Chiral Cobalt Oxide Nanoparticles for Enantiomeric Discrimination and Quantification

Xing Liu, Yanli Du, Shenli Wang, Yu Huang, Yongzhi Tian, Daniel García-Lojo, Ignacio Pérez-Juste, Jorge Pérez-Juste, Isabel Pastoriza-Santos,* and Guangchao Zheng*

Chiral transition metal oxide nanoparticles (CTMOs) are attracting a lot of attention due to their fascinating properties. Nevertheless, elucidating the chirality induction mechanism often remains a major challenge. Herein, the synthesis of chiral cobalt oxide nanoparticles mediated by histidine (Co_3O_4@L-His and Co_3O_4@D-His for nanoparticles synthesized in the presence of L- and D-histidine, respectively) is investigated. Interestingly, these CTMOs exhibit remarkable and tunable chiroptical properties. Their analysis by x-ray photoelectron, Fourier transform infrared, and ultraviolet-visible absorption spectroscopy indicates that the ratio of Co^{2+}/Co^{3+} and their interactions with the imidazole groups of histidine are behind their chiral properties. In addition, the use of chiral Co_3O_4 nanoparticles for the development of sensitive, rapid, and enantioselective circular dichroism-based sensors is demonstrated, allowing direct molecular detection and discrimination between cysteine or penicillamine enantiomers. The circular dichroism response of the chiral Co_3O_4 exhibits a limit of detection and discrimination of cysteine and penicillamine enantiomers as low as 10 μM. Theoretical calculations suggest that the ligand exchange and the coexistence of both species adsorbed on the oxide surface are responsible for the enantiomeric discrimination. This research will enrich the synthetic approaches to obtain CTMOs and enable the extension of the applications and the discovery of new chiroptical properties.

1. Introduction

The synthesis of inorganic nanomaterials with chiroptical properties has burst the development of exciting applications in the field of chiral chemo-/bio-sensing, circularly polarized photocatalysis, cancer therapy, and so on.[1–3] Typically, chiral inorganic nanostructures can be produced through the synthesis of nanoparticles (NPs) with chiral morphology or through the assembly of achiral NPs into chiral configuration.[4–10] Alternatively, the chirality transfer from chiral surface ligands to the inorganic nanostructure has also been proposed as one main route for producing NPs with chiroptical properties.[11–13] In comparison to noble metal nanomaterials (e.g., Au and Ag),[14,15] chiral transition metal oxide nanoparticles (CTMOs), such as Cu_xOS@ZIF-8,[16] ZnO,[17] $MoO_{3−x}$,[18] $WO_{3−x}$,[19] or TiO_2,[20] could show intense optical transitions from UV to near-infrared (NIR) that can be ascribed to charge transfer, plasmonic, and polaronic electronic transitions.[2] Thus, the dominant electronic transitions are responsible for the chiroptical properties.[19,21] Especially, surface atoms of CTMOs are composed of a variety of chemical states due to non-stoichiometry characteristics.[22,23] The d-band electrons of surface atoms on CTMOs make their chemical states intricate, ranging from ionic and metallic, to covalent bonds, limiting the in-depth study of the mechanism of their optical activity.[24,25]

X. Liu, Y. Du, Y. Huang, Y. Tian, G. Zheng
School of Physics and Microelectronics
Zhengzhou University
Zhengzhou 450001, P. R. China
E-mail: gczheng@zzu.edu.cn

S. Wang
School of Food Science and Engineering
Henan University of Technology
Lianhua Road 100, Zhengzhou 450001, P. R. China

D. García-Lojo, J. Pérez-Juste, I. Pastoriza-Santos
CINBIO
Universidade de Vigo
Campus Universitario As Lagoas
Marcosende, Vigo 36310, Spain
E-mail: pastoriza@uvigo.es

D. García-Lojo, I. Pérez-Juste, J. Pérez-Juste, I. Pastoriza-Santos
Departamento de Química Física
Universidade de Vigo
Campus Universitario As Lagoas
Marcosende, Vigo 36310, Spain

Theoretically, the origin of the ligand-induced chirality in CTMOs has been ascribed to two possible symmetry-breaking events: i) a ligand-induced distortion or displacement of the crystal lattice, generating "nanoscale chirality," and ii) ligand-induced interaction between chiral ligands and achiral core.[26,27] In the latter case, both orbital coupling and Coulombic interaction are primarily accepted as the main mechanism for chirality transfer.[28,29] To understand the chirality transfer mechanism, it is important to elucidate the surface chemical compositions of CTMOs as well as the interaction of the ligand with the NP surface. Mostly, amino acids or thiol-containing chiral molecules such as cysteine or penicillamine have been reported as chiral-inducing ligands because they possess amine, carboxylic acid, and thiol functionalities capable to be either covalently bound or coordinated with the surface transition metal atoms.
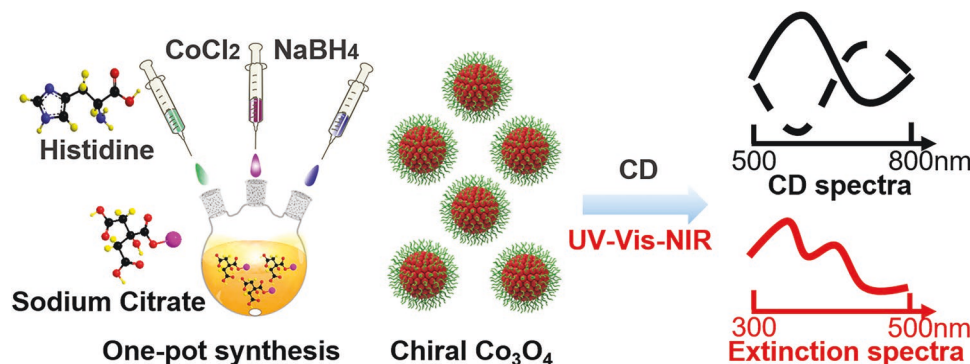
Among CTMOs, cobalt-based nanomaterials have attracted attention due to their known magnetism and structural versatility.[30,31] Thus, Kotov and co-workers reported the synthesis of paramagnetic Co_3O_4 NPs exhibiting strong chiroptical activity in the visible range mediated by L- or D-cysteine and penicillamine. Molecular dynamics simulations reveal that chiral distortions of the crystal lattices are eventually responsible for the chiroptical properties.[32] In addition, Nam et al. have studied the influence of short-chain peptides such as tyrosine-tyrosine-cysteine as ligands for the synthesis of chiral cobalt oxides.[33] Demonstrating the crucial role of the thiol group and carboxyl groups for the peptide on the evolution of the chiroptical properties indicates their strong interaction with the nanoparticle surfaces. So far, the existing studies on CTMOs have been focused on the use of single amino acids or small peptides. Particularly, in the case of Co_3O_4 NPs, only amino acids containing thiols were reported to induce chiroptical properties, highlighting the essential role of the Co—S linkage in the chirogenesis.

Here, we explored the use of histidine, an amino acid structurally similar to cysteine but with an imidazole instead of thiol functionality, as a ligand in the one-pot synthesis of Co_3O_4 NPs studying the role of the cobalt–imidazole coordination on the chiroptical response.[34] In addition, the possibility of coordination of the imidazole functionality with Co^{2+} and Co^{3+} allowed us to study the modulation of the chiroptical response in the ultraviolet-visible (UV–vis) range, as a function of the surface composition of Co_3O_4 NPs which, to the best of our knowledge, has not been reported yet. In addition, the correlation between the chiroptical properties and the surface chemical states

modulated by H_2O_2 was investigated by X-ray photoelectron spectroscopy (XPS) analysis. The results demonstrated the key role of histidine in the chiroptical response of the particles as well as the potential chiral modulation through the Co^{2+}/Co^{3+} ratio. Furthermore, we investigated the use of these chiral Co-based nanomaterials for enantiomeric sensing.

2. Results and Discussion

Chiral Co_3O_4 NPs were synthesized through a one-pot aqueous-based method previously reported but employing L- or D-histidine (L-His or D-His, respectively).[32] Briefly, to an aqueous sodium citrate solution, sodium borohydride, histidine, and cobalt chloride were added subsequently (**Scheme 1**). The color of the solution gradually changed from pink and light yellow to brown, indicating the formation of chiral Co_3O_4 NPs (denoted as Co_3O_4@L-His and Co_3O_4@D-His for nanoparticles synthesized in the presence of L-His and D-His, respectively). Transmission electron microscopy (TEM) together with dynamic light scattering (DLS) analysis revealed that the resulting Co_3O_4 NPs are very small with an average size of 1.9 and 2.2 nm, respectively (**Figure 1**a; Figure S1a, Supporting Information). To corroborate the crystalline structure of the Co_3O_4 NPs, Raman analysis of the resulting powder was performed (Figure S1b, Supporting Information), observing the characteristic Raman vibrations of the spinel Co_3O_4 structure (194, 475, and 680 cm^{-1} that correspond to $3F_{2g}$ $1E_g$ and $1A_{1g}$ Raman active modes).[35] The analysis of the chiroptical response of Co_3O_4@L-His and Co_3O_4@D-His showed a perfect mirror symmetry with two main peaks at 660 and 535 nm, assigned to different Co^{2+}/Co^{3+} intraparticle transitions (black curves in Figure 1b). However, the corresponding extinction spectra (red curves in Figure 1b) show two absorption peaks centered at 322 and 397 nm which could be assigned to transitions between surface states (including ligands) and Co^{3+}.[36] The presence of Co^{2+} and Co^{3+} was demonstrated by XPS analysis which provides information on the elemental composition. The Co 2p region of the XPS spectrum shows two spin-–orbit split lines at binding energies of 796.3 and 780.5 eV corresponding to Co $2p_{1/2}$ and Co $2p_{3/2}$, respectively. The split of the 2p orbit is 15.8 eV, a value previously reported for Co_3O_4 (Figure S2, Supporting Information).[37] In addition, two broad bands at 785.8 and 802.6 eV are attributed to their satellite shake-up peaks. Based on the

Scheme 1. Schematic representation of the one-pot synthesis of chiral Co_3O_4@His NPs.

**ADVANCED
SCIENCE NEWS**
www.advancedsciencenews.com
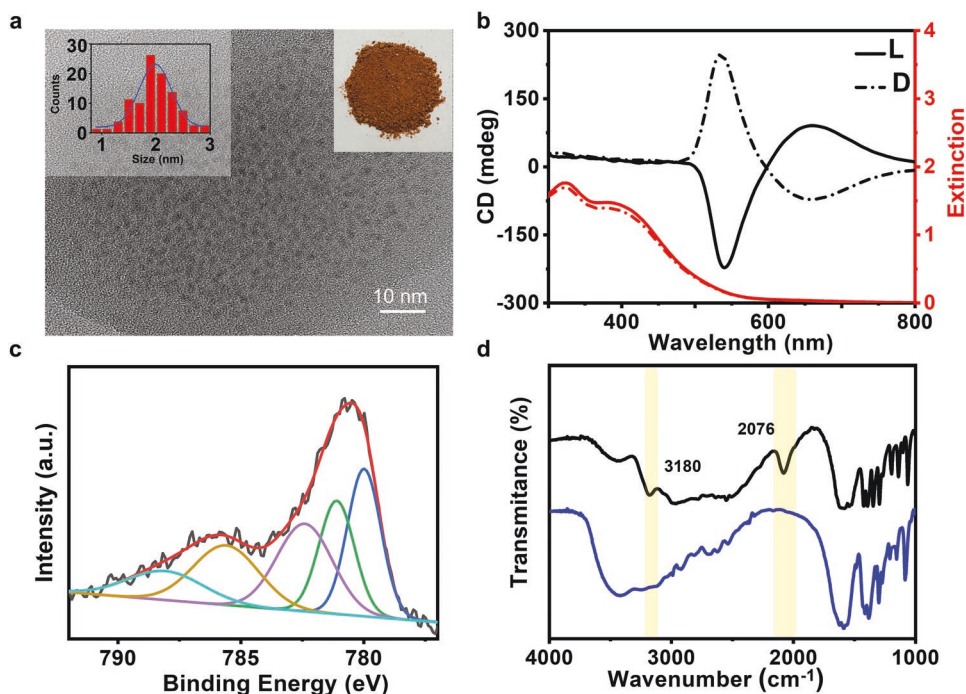
NANO · MICRO
small
www.small-journal.com

Figure 1. a) TEM image of Co_3O_4@L-His NPs. Insets: histogram showing the size distribution and a photograph of nanoparticles powder. b) CD (black) and extinction (red) spectra of Co_3O_4@L-His (solid line) and Co_3O_4@D-His (dashed line) colloids. c) Co 2p XPS spectrum of Co_3O_4@L-His, see text for details. d) Fourier transform infrared (FT-IR) spectra of L-His (black) and chiral Co_3O_4@L-His (blue) NPs. The yellow shadowed regions highlight N—H symmetric stretch vibration (3180 cm^{-1}) and C=N vibration (2076 cm^{-1}) of histidine.

previous studies,[38,39] the Co $2p_{3/2}$ peak is deconvoluted in five components 780.0, 781.2, 782.4, 785.6, and 787.6 eV attributed to Co^{2+} and Co^{3+} ions. Interestingly, the peaks at 781.1 and 782.4 eV are assigned to Co^{3+} and Co^{2+}, respectively. Last, Fourier transform infrared (FT-IR) spectroscopic analysis shows that the characteristic peaks of N—H symmetric stretch vibration (3180 cm^{-1}) and C=N vibration (2076 cm^{-1}) of His molecules are not distinguished in the FT-IR spectrum of Co_3O_4 NPs, suggesting the coordination of imidazole group and cobalt ions on the NP surface.[40] Figure 1d shows the FT-IR analysis of Co_3O_4@L-His and L-His. To get light on the chiroptical response during the growth process, time evolution analysis is performed by UV–vis–NIR and CD spectroscopies (see the details in Figure S3, Supporting Information).

To better disclose a potential mechanism of chirality transfer, different synthetic parameters such as the influence of His, cobalt ions, and sodium borohydride concentrations were evaluated. First, we studied the influence of His concentration, which imparts chirality to the NPs, while the $CoCl_2$ and $NaBH_4$ concentrations were kept constant (9.3 and 25.6 mM, respectively). With the increase in the His concentration from 6.0 to 23.3 mM, the color of solutions evolved from light yellow to brown exhibiting the characteristic absorption bands at 322 and 394 nm of cobalt oxides (**Figure 2**a). Besides, the overall increase in the intensity of the extinction spectrum suggests that the NPs yield increases with His concentration. The CD response at the lowest His concentration (6.0 mM) exhibited an intense peak at 360 nm and two weak peaks at 504 and 648 nm ascribed to the interactions of His and Co^{3+} and Co^{2+} to Co^{3+} transitions, respectively (Figure 2b). An increase in the His concentration

led to the disappearance of the peak at 360 nm and the gradual increase and red-shift of the other peaks. Regardless of the concentration, Co_3O_4@L-His and Co_3O_4@D-His showed mirror symmetry (Figure 2b). The highest g-factor at 530 nm, 0.02, was obtained at His concentration of 9.3 mM. To understand the effect of His on the chiroptical properties, we analyzed the resulting Co_3O_4 NPs by XPS. Interestingly, the XPS analysis showed that the Co^{2+}/Co^{3+} ratio gradually increases from 0.82 to 0.98 as His concentration increases (Figure S4 and Table S1, Supporting Information). This suggests that the change in the Co^{2+}/Co^{3+} ratio could affect the Co^{2+} to Co^{3+} transitions giving rise to the red-shift and increase in the intensity of the CD band located at 500–540 nm.

Second, the influence of the $NaBH_4$ concentration was also studied while keeping constant the concentrations of His and $CoCl_2$ (23.3 and 9.3 mM, respectively). As in the case of His, the variation of $NaBH_4$ concentration from 2.3 to 25.6 mM also produced higher reaction yields denoted by an increase in the extinction spectrum (Figure 2c), and a similar evolution was observed in the chiroptical response (Figure 2d). In addition, the initial bands at 497 nm (positive) and 666 nm (negative) evidenced for 2.3 mM $NaBH_4$ gradually red-shifted and increased in intensity as the amount of $NaBH_4$ increased. A further increase in the $NaBH_4$ concentration (above 16.3 mM) did not produce any significant changes in the optical response. This behavior can be explained considering the role of $NaBH_4$ as a basifying agent because pH above 8 is needed to deprotonate the amine groups of aminoacids and favour its coordination with cobalt.[12] In fact, the use of NaOH as an alternative to $NaBH_4$ as a basic agent gave rise to similar results (Figure S5,
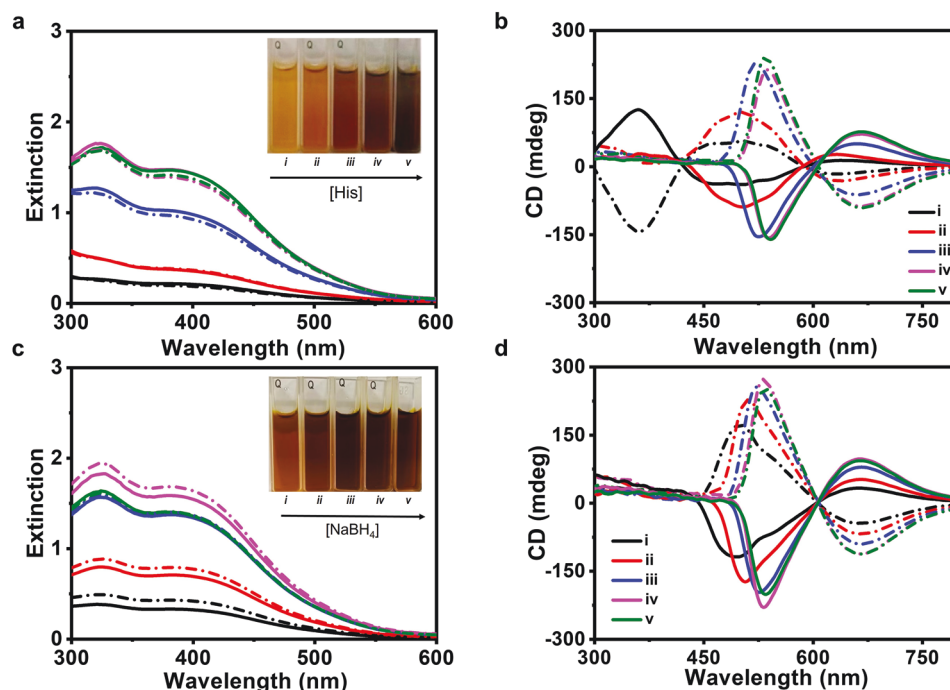
Figure 2. a) Extinction and b) CD spectra of Co_3O_4@L-His (solid) and Co_3O_4@D-His (dashed) NPs obtained with different [His]: i) 6.0 mм; ii) 9.3 mм; iii) 15.1 mм; iv) 23.3 mм, and v) 34.9 mм. [$CoCl_2$] and [$NaBH_4$] were 9.3 and 25.6 mм, respectively. c) Extinction and d) CD spectra of Co_3O_4@L-His (solid) and Co_3O_4@D-His (dashed) NPs obtained with different [$NaBH_4$]: i) 2.3 mм, ii) 7.0 mм, iii) 16.3 mм, iv) 25.6 mм, and v) 51.2 mм. [His] and [$CoCl_2$] were 23.3 and 9.3 mм, respectively.

Supporting Information), while under neutral conditions, the reaction yield was very low (low absorbance). Nevertheless, the XPS analysis of Co_3O_4 NPs revealed that the Co^{2+}/Co^{3+} ratio increased with the $NaBH_4$ concentration from 0.85 to 0.99 (Figure S6 and Table S2, Supporting Information). This result suggests that the observed red-shift of CD peaks could be ascribed to changes in the d–d excitations from Co^{2+} to Co^{3+}.

Last, the influence of the cobalt chloride concentration was also studied while keeping constant the concentrations of His and $NaBH_4$ (23.3 and 25.6 mм, respectively). The results found that the Co_3O_4 particle yield increased with the cobalt chloride concentration as indicated by the increase in the extinction spectra (Figure S7, Supporting Information). It was also accompanied by a red shift and an increase in the main chiral band located at 490 nm. The XPS analysis of the $2p_{3/2}$ band showed that the Co^{2+}/Co^{3+} ratio increased from 0.88 to 0.99 with the $CoCl_2$ concentration (Figure S8 and Table S3, Supporting Information), suggesting that the percentage of Co^{3+} present could be responsible for the red-shift and increase in the intensity of the main CD band located in the visible region.

Overall, the analysis of the different synthetic parameters seems to indicate that the Co^{2+}/Co^{3+} ratio is the key factor controlling the chiroptical response of the Co_3O_4 NPs. To further confirm the effect of surface compositions on the chiroptical response of chiral Co_3O_4 NPs, a strong oxidizing agent such as H_2O_2 was injected into pre-synthesized chiral Co_3O_4 NPs. **Figure 3** shows the extinction and CD spectra of Co_3O_4@L-His (solid lines) and Co_3O_4@D-His (dashed lines) after the addition of different amounts of H_2O_2. In general, H_2O_2 produced a decrease in the characteristic extinction bands and a

clear blue shift of the CD peaks in the visible region, being proportional to the H_2O_2 concentration. Besides, at [H_2O_2] higher than 16.4 mм, the appearance of CD peak at 382 nm attributed to Co^{2+} to Co^{3+} transitions is observed.[32] The XPS analysis showed that the Co^{2+}/Co^{3+} ratio decreases from 0.98 to 0.66 as the H_2O_2 concentration increases (Figure S9 and Table S4, Supporting Information), suggesting the key role of the Co^{2+}/Co^{3+} ratio in the chiroptical response of Co_3O_4 NPs. Thus, the addition of H_2O_2 produces the partial oxidation of Co^{2+} to Co^{3+} giving rise to chiroptical properties in the visible range, ascribed to changes in the d–d excitations from Co^{2+} to Co^{3+}.

Next, to provide an in-depth understanding of the enantioselective interaction of α-amino acids with the chiral Co_3O_4 NPs, a series of α-amino acids with different functional moieties was investigated. More precisely, we focused on amine, thiol, and imidazole functionalities which present coordination capabilities with cobalt ions. Thus, for the tested α-amino acids containing solely an amine functional group (L-leucine, L-valine, L-phenylalanine, L-methionine, and L-tryptophan), none of them gave rise to chiral Co_3O_4 NPs (Figures S10 and S11, Supporting Information). Interestingly, when amino acids contained either thiol (cysteine or penicillamine) or imidazole (histidine) groups, the resulting Co_3O_4 NPs exhibited chiroptical properties (Figures S12 and S13, Supporting Information). Taking into account the different interactions of the functional groups with the inorganic surfaces, a different ligand configuration on the interface was expected; and therefore, different chiroptical properties.

In the present case, to the best of our knowledge, this is the first demonstration that imidazole functionality could also
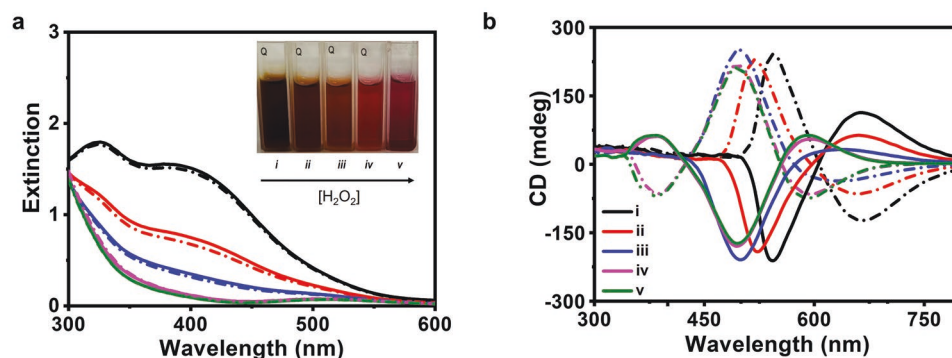
Figure 3. a) Extinction and b) CD spectra of Co_3O_4@L-His (solid) and Co_3O_4@D-His (dashed) NPs after the addition of different $[H_2O_2]$: i) 0 mм, ii) 3.3 mм, iii) 6.6 mм, iv) 16.4 mм, and v) 62.5 mм. $[CoCl_2]$ = 9.3 mм, $[NaBH_4]$ = 25.6 mм, and [His] = 23.3 mм. Inset: photograph of the resulting Co_3O_4 colloids.

induce chiroptical properties in Co_3O_4 NPs. We propose that the origin of the chirality and its tunability arise from the relatively low-high stability and the slow-fast ligand exchange in the primary coordination sphere of Co^{2+} and Co^{3+} ions with imidazole groups.[41] Thus, Wegner et al. demonstrated that Co^{3+} complexes have significantly higher formation constants than Co^{2+} complexes in similar coordination environments and proposed Co^{3+} as a stable and inert mediator ion between nitrilotriacetic acid (NTA) and histidine-tagged proteins.[41] In addition, as the formation of Co^{3+} complexes is very slow, they proposed an indirect method in which the metal center was oxidized in situ through the exchange-labile divalent Co^{2+}.[41] We strongly believe that in the present case, the combination of the cobalt ion complexation with the imidazole and amine functional groups of histidine,[42] together with exchange-labile divalent Co^{2+} and the highly stable Co^{3+} complexes, are responsible for the chiroptical tunability of the Co_3O_4 NPs. This assumption is supported by the CD spectra variation and the Co^{2+}/Co^{3+} ratio composition when chiral Co_3O_4@L-His NPs are treated with different H_2O_2 concentrations (Figure 3; Figure S5, Supporting Information). In addition, the CD response of Co_3O_4@L-Cys NPs is not affected by H_2O_2 (Figure S14, Supporting Information), which could be attributed to the low exchangeability of Co^{2+}/Co^{3+} when complexed with thiolated amino acids.

The detection and resolution of enantiomers are of key importance in chirality applications.[43] Thus, enantiomeric drugs or amino acids exhibit distinct physiological properties, toxicities, and metabolic routes.[44] Chiroptical signals of biomolecules are typically localized in the UV range. Although CD spectroscopy has commonly been applied for the discrimination of enantiomers, the need for high concentration due to the weak CD signals, limited their further identification and deep research (Figure S15, Supporting Information). Herein, we explored the highly labile surface chemistry of chiral Co_3O_4@L-His and Co_3O_4@D-His NPs as a chemical probe to differentiate between enantiomers. Thus, chiral Co_3O_4@L-His and Co_3O_4@D-His NPs exhibiting CD peaks at 354, 453, 505, and 550 nm (**Figure 4**a) were tested for D-Pen sensing. As shown in Figure 4a, the main CD peak of Co_3O_4LHis at 357 nm decreased and red-shifted as the concentration of D-Pen increased. Interestingly, the variation of the wavelength position of the main CD peak followed a linear dependence

with the increase of D-Pen concentration (Figure 4c). Figure 4a shows an overall decrease in the main chiral peak of Co_3O_4@D-His NPs with increasing the D-Pen concentration but without affecting its wavelength position (Figure 4c). To demonstrate the enantioselective interaction, Co_3O_4@D-His NPs were also analyzed for L-Pen sensing. Similar results were obtained when Co_3O_4@L-His and Co_3O_4@D-His NPs were tested for L-Pen sensing. Thus, a decrease and a linear red shift in the main CD peak of Co_3O_4@D-His NPs were observed with the increase in L-Pen concentration (Figure 4b; Figure S16, Supporting Information). However, the main CD peak did not shift when investigating the chiral response of Co_3O_4@L-His NPs in the presence of L-Pen (Figure 4b; Figure S13, Supporting Information). Remarkably, an L-Pen or D-Pen concentration as low as 10 µм can be easily discriminated by simply analyzing the variation of the CD response of Co_3O_4@L-His and Co_3O_4@D-His NPs. Similar results were also obtained for the discrimination of cysteine enantiomers (Figure S17, Supporting Information). Unfortunately, such enantiomer discrimination was not observed for other α-amino acids without thiol motifs (such as Aspartic acids, Valine, or Tryptophan), where only a decrease in the main CD peak was observed with the amino acid concentration (Figure S18, Supporting Information). Therefore, the results suggest that enantiomeric discrimination and quantification of α-amino acids with thiol functionalities with chiral Co_3O_4@His NPs could be ascribed to the labile surface chemistry of the histidine-coordinated Co^{2+} and Co^{3+} surface atoms. The thermodynamically stable complex between Co^{3+} and imidazole makes it inert toward ligand exchange and not to react with chelators or reducing agents, such as thiols.[41]

To better understand the nature of chirality transfer and chirality-based enantiomeric sensing, we investigated the surface interaction between Co_3O_4 NPs and L-His or L-Pen through atomic scale dynamics. First, we performed a conformational analysis of L-His as it exhibits high molecular flexibility (Figure S19, Supporting Information). It should be noted that a similar analysis is not necessary for the D-His because the calculated absorption and CD response for both enantiomers are mirror images. To study the L-His-Co_3O_4 NPs interaction, we considered the adsorption of a single molecule on a Co_3O_4 {110} slab (denoted as L-His-Co_3O_4 {110}) and performed geometrical optimizations of many different initial L-His configurations on
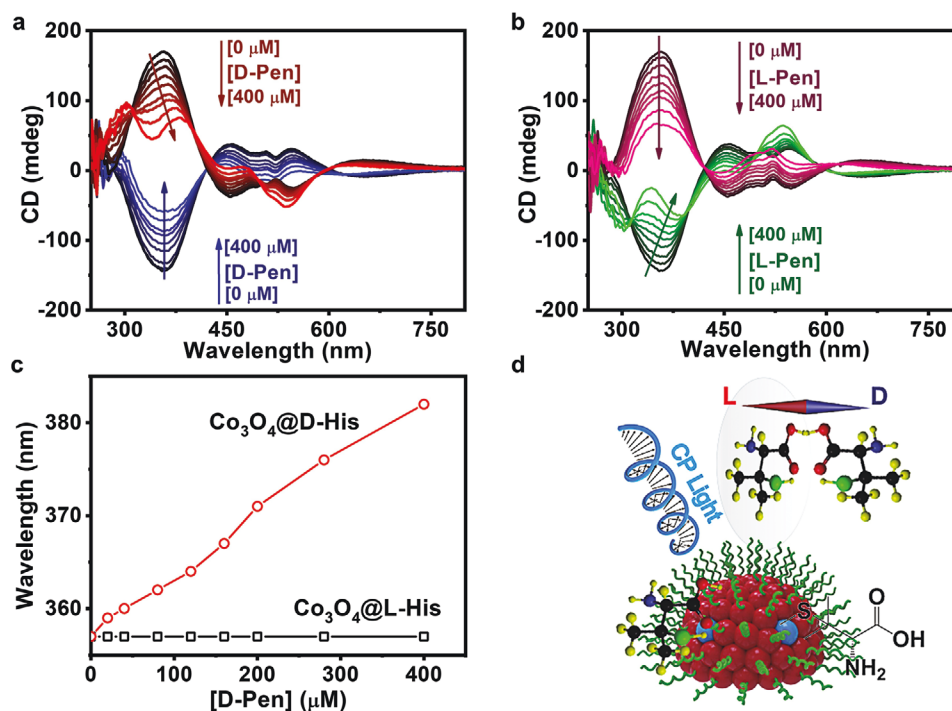
Figure 4. Enantiomeric identification and quantification of Pen based on the CD response of chiral Co_3O_4@His. a) CD spectra of chiral Co_3O_4@L-His (red curves) and Co_3O_4@D-His (blue curves) NPs in the presence of different concentrations of D-Pen. b) CD spectra of chiral Co_3O_4@L-His (pink curves) and Co_3O_4@D-His (green curves) NPs in the presence of different concentrations of L-Pen. c) Variation of the main CD peak position of chiral Co_3O_4@His, as indicated, with the concentration of D-Pen. d) Cartoon of enantiomeric sensing of Pen by chiral Co_3O_4@His.

the surface. According to the results obtained, the interaction between L-His and Co_3O_4 takes place simultaneously through several sites, that is, the nitrogen atoms of the imidazole ring, the nitrogen atom of the NH_2 unit, and the oxygen atoms of the carbonyl group, being slightly more favourable, the interaction is through the nitrogen atom of the imidazole ring with octahedral Co^{3+} than with tetrahedral Co^{2+} atoms. Next, the most stable configuration, shown in **Figure 5**a, was employed to predict the electronic CD spectrum by applying the tight-binding based simplified Tamm–Dancoff approximation (sTDA-xTB) method. Even though the experimental CD response corresponds to a combination of many configurations interchanging in time, the overall agreement with the calculated CD spectrum obtained for a single configuration (see Figure S20, Supporting Information) is very good. It indicates that this theoretical model is remarkable enough to study the interaction between L-His and the Co_3O_4 surface. Thus, theory predicts that the CD spectrum of L-His adsorbed on Co_3O_4 extends until the visible region and is dominated by a positive CD signal at ≈330 nm (which can be associated with the experimental signal at 360 nm) and two additional negative signals around 440 and 630 nm (which can be related with the experimental signals at 504 and 648 nm, respectively). It must be noted here that a similar CD spectrum has been reported from theoretical calculations employing a smaller model for the interaction between histidine and cobalt.[45]

Next, we investigated what electronic transitions are behind the observed theoretical CD features (Figure S21 and Table S5, Supporting Information) by computing the first 350 electronic transitions using time-dependent density functional theory

(TDDFT). Thus, the positive CD signal at lower wavelengths around 330 nm and the negative CD signal around 400 nm can be assigned a ligand to cluster transition. However, the electronic transition associated with the CD band around 500 nm is accompanied by an increase in the electronic density of L-His as a consequence of metal to ligand transition. Last, the less energetic electronic transitions appearing at longer wavelengths are probably associated with electronic transitions mostly located in the oxide.

To get insight into the experimental changes observed upon L- or D-Pen addition to the Co_3O_4@L-His system, we performed on L-Pen a similar theoretical study as with L-His (see Figures S22–S24 and Table S6, Supporting Information). As in the previous case, the similarities between the experimental and theoretical data are quite remarkable (Figure S23, Supporting Information). Interestingly, the adsorption energy of the most stable configuration is defined as:

$$E_{ads} = E\left(L-Pen-Co_3O_4\{110\}\right) - E\left(Co_3O_4\{110\}\right) - E\left(L-Pen\right) \quad (1)$$

where E(L-Pen-Co_3O_4\{110\}), E(Co_3O_4\{110\}), and E(L-Pen) are the total energy of the L-Pen-Co_3O_4\{110\} complex slab, the energy of the Co_3O_4\{110\} slab, and the energy of the most stable L-PEN conformer, respectively. The calculated value of E_{ads} was −132.4 kcal mol^{-1} which was notably larger than the corresponding value for L-His (−87.8 kcal mol^{-1}), suggesting that adsorption of L-Pen on the oxide surface is preferred over the adsorption of L-His.

Based on the large difference in adsorption energies for L-His and L-Pen, we can assume that the enantiomeric
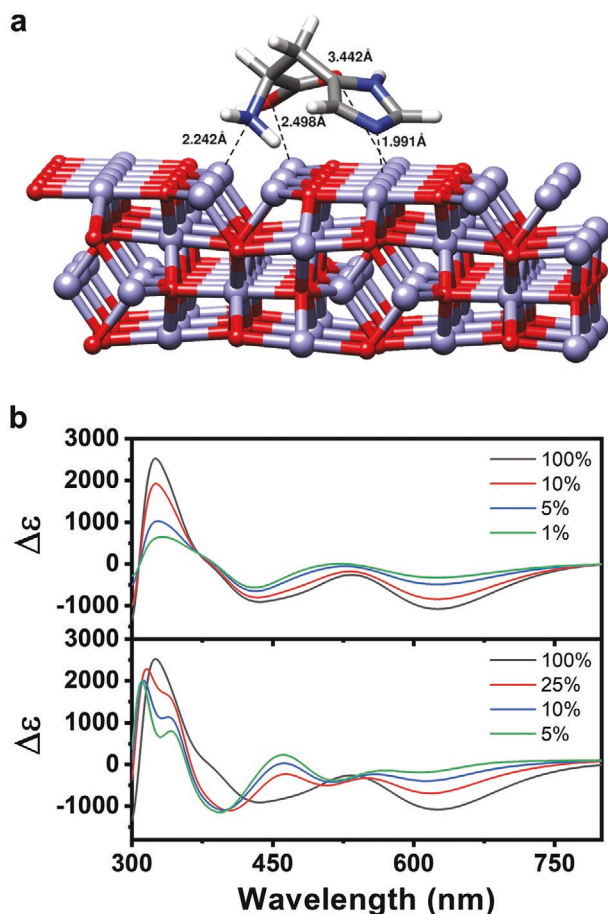
a

b

Figure 5. a) Schematic representation of the most stable configuration for the adsorption of L-His on a Co_3O_4 {110} slab. The main interatomic distances between L-His and the surface cobalt atoms are indicated. b) CD spectra obtained from combinations of different proportions of the theoretical spectra of L-His-Co_3O_4 {110} and L-Pen-Co_3O_4 {110} systems (top) and L-His-Co_3O_4 {110} and D-Pen-Co_3O_4 {110} systems (bottom). The labels indicated the proportions of the L-His-Co_3O_4 {110} system in each combination.

discrimination based on the CD response arises from the exchange of L-His surface ligands by either the L- or D-Pen ligands. Thus, we have analyzed the changes in the CD profiles when combining the computed CD spectrum of L-His-Co_3O_4 {110} (see black spectrum in Figure 5b) with increasing proportions of the computed profile for the L-Pen-Co_3O_4 {110} system (Figure S23, Supporting Information). Figure 5b shows the theoretical CD spectra obtained at different decreasing L-His-Co_3O_4 {110} proportions from 100% to 90%. Interestingly, the results obtained agreed with the enantiomeric identification experiments in Figure 4b where an overall decrease of the main CD peak located around 350 nm was observed. To further mimic the experimental data, in Figure 5b (bottom), we also computed the CD profiles for combinations of the CD spectrum for L-His-Co_3O_4 {110} with increasing proportions of the computed spectrum for the D-Pen-Co_3O_4 {110} (Figure S25, Supporting Information). Remarkably, the theoretical CD profiles for these combinations also agree reasonably well with the experimental ones showing the distinctive pattern at lower

wavelengths observed in the experiments (see Figure 4a). The good agreement between the experimental data and the theoretical calculations suggested that the ligand exchange and the coexistence of both species adsorbed on the oxide surface were responsible for the CD-based enantiomeric discrimination.

3. Conclusion

In summary, chiral cobalt oxide nanoparticles with a g-factor as high as 0.02 in the visible range were synthesized using histidine as ligand. The influence of different parameters in the chirality response was investigated and the synthetic conditions were optimized through experimental demonstration, showing an optical response covering UV to the visible range. In addition, FT-IR and XPS analysis revealed that the imidazole group of histidine interacts with the nanoparticle surface suggesting that the origin of the chirality and its tunability arise from the relatively low–high stability and the slow–fast ligand exchange in the primary coordination sphere of Co^{2+} and Co^{3+} ions with imidazole groups. Furthermore, the labile surface chemistry of the histidine-coordinated Co^{2+} and Co^{3+} surface atoms allows the chirality-dependent detection and discrimination of enantiomers. Moreover, theoretical calculations demonstrate that the origin of the CD-based enantiomeric discrimination arises from the exchange between ligands and the coexistence of both species adsorbed on the oxide surface, providing new insights for the development of chiral-based sensors.

4. Experimental Section

Materials: Cobalt chloride ($CoCl_2$, 99.99%), Sodium borohydride ($NaBH_4$, 98%), Sodium citrate (99%), L-Histidine (L-His, 99%), D-Histidine (D-His, 99%), L-Cysteine (L-Cys, 97%), D-Cysteine (D-Cys, 98%), L-Penicillamine (L-Pen, 99%), D-Penicillamine (D-Pen, 98%), and other amino acids were purchased from Adamas.

Synthesis of Chiral Cobalt Oxides: Synthesis of chiral cobalt oxides followed a previous report.[16] Sequentially 400 µL of sodium citrate (0.1 M), 1.1 mL of $NaBH_4$ (0.1 M), 1 mL of L- or D-His (0.1 M), and 200 µL of $CoCl_2$ (0.2 M) were injected into 1.6 mL aqueous solution. After stirring for 3 h and letting stand for 12 h at room temperature, chiral Co_3O_4@His NPs were obtained by centrifugation (8000 rpm; 20 min) with isopropanol added seven times its volume. The obtained NPs were stored in 5 mL of water. Following this protocol, a series of chiral cobalt oxides capping with different amino acids was obtained.

Racemic Sensing of Amino Acids: A certain volume of enantiomers of amino acids was quickly injected into 5 mL of chiral cobalt oxides solutions, quickly stirred at 500 rpm for 5 min. Afterward, the solutions were immediately measured by CD and extinction spectra.

Characterization: The CD measurements of chiral cobalt oxides were recorded with J-810 spectrophotometer (JASCO, Japan). The extinction spectrum was carried out by the UV-1900 (SHIMADZU). Transmission electron microscopy (TEM, JEM-2010, 200 kV). The composition of the NPs was verified by X-ray photoelectron spectra (XPS, Thermo SCIENTIFIC Nexsa) with monochromatic Al k-alpha radiation with an energy of 1486.68 eV and a voltage of 12 000 V; a current of 6 mA, a vacuum degree of less than 10^{-9} mbar, and a pass energy of 200 eV. Dynamic light scattering experiments to determine the hydrodynamic diameter were carried out on a Zetasizer Nano S (Malvern Instruments, Malvern UK).

Raman characterization of nanoparticles powder was carried out using a Renishaw InVia Reflex system. The spectrograph used a

ADVANCED
SCIENCE NEWS

www.advancedsciencenews.com

NANO · MICRO
small

www.small-journal.com

high-resolution grating (1200 grooves/cm) with additional band-pass filter optics, a confocal microscope, and a 2D-CCD camera. Laser excitation was carried out employing a 50× objective (N.A. 0.75) with an excitation wavelength of 785 nm (3.98 mW) with an acquisition time of 20 s and two accumulations. The spectra were acquired using WiRE Software v. 4.3 (Renishaw, UK).

Computational Methods: Initial gas phase conformational analysis of L-Histidine (L-His) and the thiolate form of L-penicillamine (L-Pen) have been performed employing DFT methods with the M062X functional, the 6-311+G* basis set for C, H, N, O and S, and the LANL2DZ basis set with the LANL2DZ pseudo potential for Co. Geometrical optimization of the possible staggered conformers had been performed and energy minima were characterized by computation of their harmonic vibrational frequencies using Gaussian16.

As a model for studying the adsorption of a single L-His/L-Pen molecule on the Co_3O_4 surface, a four-layer slab of the {110} surface of 16.3×17.3 Å^2 containing 168 atoms from the crystal structure of the oxide was built up. Two main reasons justify the choice of this model: On the one hand, the exposed {110} surface of the slab was composed by Co^{2+} and Co^{3+} atoms tetrahedrally and octahedrally coordinated with oxygen atoms, respectively. This mixture allowed the authors to explore the different interactions between the adsorbed molecules and Co^{2+} and Co^{3+} atoms. On the other hand, the {110} facet presented a zero magnetic moment along the surface plane and the even number of atoms assured that the slab was a closed shell system without unpaired electrons.[46] Both conditions minimized the possible effect of the magnetic properties of the cobalt oxide which were beyond the authors' experiment study and theoretical computations.

To explore the interaction between L-His and L-Pen with the Co_3O_4 surface, the GFN2-xTB density functional tight-binding method[47] was employed with periodic boundary conditions as implemented in the DFTB+ program.[48] The size of the supercell, 16.3×17.3 Å^2 with a vacuum layer over the top surface of 25 Å, was large enough to avoid molecular lateral interactions and geometrical optimizations were obtained taking only into account the Γ-point. The geometries of many different initial configurations of L-His and L-Pen over the surface were optimized while keeping fixed the structure of the oxide. Last, CD spectra of the optimized configurations were computed employing the simplified Tamm–Dancoff approximation specifically derived for xTB computations and implemented in the sTDA-xTB program.[49]

To obtain a deeper insight about the electronic transitions giving rise to the CD signals, two smaller models comprising the previously optimized geometries of L-His/L-Pen on a two-layer cluster of Co_3O_4 (39 and 45 atoms, respectively) were considered. The CD spectra for these smaller systems were obtained by computation of their first 350 electronic transitions using TDDFT calculations at the M062X/6-311+G*/LANL2DZ level with Gaussian16. Usually, transitions between electronic states in complex systems such as those studied here were not dominated by a single transition between molecular orbitals and many molecular orbital pairs could contribute simultaneously to a given electron transition, hindering the analysis and characterization of the electron excitations. For this reason, the nature of the main electronic transitions for these small clusters had been analyzed by means of their natural transition orbitals (NTOs). The NTO method performed a separated unitary transformation for occupied and virtual molecular orbitals; so that, only one or few NTO pairs are necessary to describe any electronic transition, providing an easier-to-interpret picture of electronic excitation.[50] Last, the interfragment charge transfer (IFCT) method implemented in Multiwfn which allowed the calculation of the amount of charge transferred between any number of fragments in a complex system during an electron excitation process was also employed. The evaluation of this IFCT charge transfer, based on the description of an electronic transition as a hole→electron process between an initial (ground state) and a final (excited state) electronic distribution, provides information about the contribution of each defined fragment to the hole and electron densities as well as the amount of charge transfer between fragments. In the systems studied here, the first fragment corresponds to the LHis/LPen molecule, while the oxide cluster corresponds to

the second one. Both the NTOs and the IFCT values were obtained employing the 3.8 version of the Multiwfn program.[51]

Supporting Information

Supporting Information is available from the Wiley Online Library or from the author.

Conflict of Interest

The authors declare no conflict of interest.

Data Availability Statement

The data that support the findings of this study are available from the corresponding author upon reasonable request.

[1] G. C. Zheng, J. J. He, V. Kumar, S. L. Wang, I. Pastoriza-Santos, J. Perez-Juste, L. M. Liz-Marzan, K. Y. Wong, *Chem. Soc. Rev.* **2021**, *50*, 3738.

[2] J. C. Fan, N. A. Kotov, *Adv. Mater.* **2020**, *32*, 1906738.

[3] W. Ma, L. G. Xu, A. F. de Moura, X. L. Wu, H. Kuang, C. L. Xu, N. A. Kotov, *Chem. Rev.* **2017**, *117*, 8041.

[4] G. Gonzalez-Rubio, J. Mosquera, V. Kumar, A. Pedrazo-Tardajos, P. Llombart, D. M. Solis, I. Lobato, E. G. Noya, A. Guerrero-Martinez, J. M. Taboada, F. Obelleiro, L. G. MacDowell, S. Bals, L. M. Liz-Marzan, *Science* **2020**, *368*, 1472.

[5] H. E. Lee, H. Y. Ahn, J. Mun, Y. Y. Lee, M. Kim, N. H. Cho, K. Chang, W. S. Kim, J. Rho, K. T. Nam, *Nature* **2018**, *556*, 360.

[6] J. W. Lv, X. Q. Gao, B. Han, Y. F. Zhu, K. Hou, Z. Y. Tang, *Nat. Rev. Chem.* **2022**, *6*, 125.

[7] X. Lan, X. X. Lu, C. Q. Shen, Y. G. Ke, W. H. Ni, Q. B. Wang, *J. Am. Chem. Soc.* **2015**, *137*, 457.

[8] Y. Y. Duan, X. Liu, L. Han, S. Asahina, D. D. Xu, Y. Y. Cao, Y. Yao, S. N. Che, *J. Am. Chem. Soc.* **2014**, *136*, 7193.

[9] S. H. Liu, L. Han, Y. Y. Duan, S. Asahina, O. Terasaki, Y. Y. Cao, B. Liu, L. G. Ma, J. L. Zhang, S. A. Che, *Nat. Commun.* **2012**, *3*, 1215.

[10] G. C. Zheng, S. L. Jiao, W. Zhang, S. L. Wang, Q. H. Zhang, L. Gu, W. X. Ye, J. J. Li, X. C. Ren, Z. C. Zhang, K. Y. Wong, *Nano Res.* **2022**, *15*, 6574.

[11] W. J. Liu, Z. N. Zhu, K. Deng, Z. T. Li, Y. L. Zhou, H. B. Qu, Y. Gao, S. N. Che, Z. Y. Tang, *J. Am. Chem. Soc.* **2013**, *135*, 9659.

[12] J. Y. Lin, R. L. Liu, X. Zhu, A. Wei, X. Q. Xu, T. C. He, J. J. Cheng, Y. W. Li, *Small* **2022**, *18*, 2107570.

[13] A. Ben-Moshe, B. Maoz, A. O. Govorov, G. Markovich, *Chem. Soc. Rev.* **2013**, *42*, 7028.

[14] G. C. Zheng, Z. Y. Rao, J. Perez-Juste, R. L. Du, W. Liu, J. Y. Dai, W. Zhang, L. Y. S. Lee, K. Y. Wong, *Angew. Chem., Int. Ed.* **2018**, *57*, 16452.

[15] J. Q. Chen, X. S. Gao, Q. Zheng, J. B. Liu, D. J. Meng, H. Y. Li, R. Cai, H. Z. Fan, Y. L. Ji, X. C. Wu, *ACS Nano* **2021**, *15*, 15114.

[16] A. M. Yuan, C. L. Hao, X. L. Wu, M. Z. Sun, A. H. Qu, L. G. Xu, H. Kuang, C. L. Xu, *Adv. Mater.* **2020**, *32*, 1906580.

[17] Y. Y. Duan, L. Han, J. L. Zhang, S. Asahina, Z. H. Huang, L. Shi, B. Wang, Y. Y. Cao, Y. Yao, L. G. Ma, C. Wang, R. K. Dukor, L. Sun, C. Jiang, Z. Y. Tang, L. A. Nafie, S. N. Che, *Angew. Chem., Int. Ed.* **2015**, *54*, 15170.

[18] Y. W. Li, Z. W. Miao, Z. W. Shang, Y. Cai, J. J. Cheng, X. Q. Xu, *Adv. Funct. Mater.* **2020**, *30*, 1906311.

[19] S. Jiang, M. Chekini, Z. B. Qu, Y. C. Wang, A. Yeltik, Y. G. Liu, A. Kotlyar, T. Y. Zhang, B. Li, H. V. Demir, N. A. Kotov, *J. Am. Chem. Soc.* **2017**, *139*, 13701.

[20] T. D. Nguyen, J. Li, E. Lizundia, M. Niederberger, W. Y. Hama, M. J. MacLachlan, *Adv. Funct. Mater.* **2019**, *29*, 1904639.

[21] J. T. Collins, C. Kuppe, D. C. Hooper, C. Sibilia, M. Centini, V. K. Valev, *Adv. Opt. Mater.* **2017**, *5*, 1700182.

[22] M. T. Greiner, L. Chai, M. G. Helander, W. M. Tang, Z. H. Lu, *Adv. Funct. Mater.* **2012**, *22*, 4557.

[23] D. Neagu, G. Tsekouras, D. N. Miller, H. Menard, J. T. S. Irvine, *Nat. Chem.* **2013**, *5*, 916.

[24] M. T. Greiner, M. G. Helander, W. M. Tang, Z. B. Wang, J. Qiu, Z. H. Lu, *Nat. Mater.* **2012**, *11*, 76.

[25] D. O. Scanlon, G. W. Watson, D. J. Payne, G. R. Atkinson, R. G. Egdell, D. S. L. Law, *J. Phys. Chem. C* **2010**, *114*, 4636.

[26] A. O. Govorov, Z. Y. Fan, P. Hernandez, J. M. Slocik, R. R. Naik, *Nano Lett.* **2010**, *10*, 1374.

[27] Y. W. Li, J. J. Cheng, J. G. Li, X. Zhu, T. C. He, R. Chen, Z. K. Tang, *Angew. Chem., Int. Ed.* **2018**, *57*, 10236.

[28] Y. W. Li, X. B. Wang, J. Miao, J. G. Li, X. Zhu, R. Chen, Z. K. Tang, R. K. Pan, T. C. He, J. J. Cheng, *Adv. Mater.* **2020**, *32*, 1905585.

[29] O. Cleary, F. Purcell-Milton, A. Vandekerckhove, Y. K. Gun'ko, *Adv. Opt. Mater.* **2017**, *5*, 1601000.

[30] S. Li, L. Xu, M. Lu, M. Sun, L. Xu, C. Hao, X. Wu, C. Xu, H. Kuang, *Nano Res.* **2021**, *14*, 2451.

[31] C. Li, S. Li, J. Zhao, M. Z. Sun, W. W. Wang, M. R. Lu, A. H. Qu, C. L. Hao, C. Chen, C. L. Xu, H. Kuang, L. G. Xu, *J. Am. Chem. Soc.* **2022**, *144*, 1580.

[32] J. Yeom, U. S. Santos, M. Chekini, M. Cha, A. F. de Moura, N. A. Kotov, *Science* **2018**, *359*, 309.

[33] H. Kim, K. M. Bang, H. Ha, N. H. Cho, S. D. Namgung, S. W. Im, K. H. Cho, R. M. Kim, W. Il Choi, Y. C. Lim, J. Y. Shin, H. K. Song, N. K. Kim, K. T. Nam, *ACS Nano* **2021**, *15*, 979.

[34] M. S. Seo, K. Kim, H. Kim, *Chem. Commun.* **2013**, *49*, 11623.

[35] G. X. Wang, X. P. Shen, J. Horvat, B. Wang, H. Liu, D. Wexler, J. Yao, *J. Phys. Chem. C* **2009**, *113*, 4357.

[36] F. Gu, C. Z. Li, Y. J. Hu, L. Zhang, *J. Cryst. Growth* **2007**, *304*, 369.

[37] R. M. Mohamed, A. A. Ismail, A. S. Basaleh, H. A. Bawazir, *J. Photochem. Photobiol.* **2022**, *428*, 113859.

[38] M. C. Biesinger, B. P. Payne, A. P. Grosvenor, L. W. M. Lau, A. R. Gerson, R. S. Smart, *Appl. Surf. Sci.* **2011**, *257*, 2717.

[39] Z. Chen, C. X. Kronawitter, B. E. Koel, *Phys. Chem. Chem. Phys.* **2015**, *17*, 29387.

[40] S. Sharma, M. Chauhan, A. Jamsheera, S. Tabassum, F. Arjmand, *Inorg. Chim. Acta* **2017**, *458*, 8.

[41] S. V. Wegner, J. P. Spatz, *Angew. Chem., Int. Ed.* **2013**, *52*, 7593.

[42] W. Jiang, Q. Xu, X. H. Wei, *J. Hazard. Mater.* **2019**, *374*, 50.

[43] R. Noyori, *Angew. Chem., Int. Ed.* **2002**, *41*, 2008.

[44] E. L. Izake, *J. Pharm. Sci.* **2007**, *96*, 1659.

[45] S. Y. Xiao, J. C. Liang, J. Z. Li, J. J. Cheng, X. Zhu, T. C. He, *Nanoscale* **2022**, *14*, 15414.

[46] R. A. P. Ribeiro, S. R. de Lazaro, L. Gracia, E. Longo, J. Andres, *J. Magn. Magn. Mater.* **2018**, *453*, 262.

[47] C. Bannwarth, E. Caldeweyher, S. Ehlert, A. Hansen, P. Pracht, J. Seibert, S. Spicher, S. Grimme, *Wiley Interdiscip. Rev. IREs: Comput. Mol. Sci.* **2021**, *11*, e1493.

[48] B. Hourahine, B. Aradi, V. Blum, F. Bonafe, A. Buccheri, C. Camacho, C. Cevallos, M. Y. Deshaye, T. Dumitrica, A. Dominguez, S. Ehlert, M. Elstner, T. van der Heide, J. Hermann, S. Irle, J. J. Kranz, C. Kohler, T. Kowalczyk, T. Kubar, I. S. Lee, V. Lutsker, R. J. Maurer, S. K. Min, I. Mitchell, C. Negre, T. A. Niehaus, A. M. N. Niklasson, A. J. Page, A. Pecchia, G. Penazzi, et al., *J. Chem. Phys.* **2020**, *152*, 124101.

[49] S. Grimme, C. Bannwarth, *J. Chem. Phys.* **2016**, *145*, 054103.

[50] R. L. Martin, *J. Chem. Phys.* **2003**, *118*, 4775.

[51] T. Lu, F. W. Chen, *J. Comput. Chem.* **2012**, *33*, 580.